npj | 2D materials and applications

www.nature.com/npj2dmaterials

ARTICLE OPEN

Check for updates

Tunable strain and bandgap in subcritical-sized MoS_2 nanobubbles

Michele Gastaldo[1,4], Javier Varillas[1,2,4], Álvaro Rodríguez[1,3], Matěj Velický[1], Otakar Frank[1] and Martin Kalbáč[1]✉

Nanobubbles naturally formed at the interface between 2D materials and their substrate are known to act as exciton recombination centers because of the reduced bandgap due to local strain, which in turn scales with the aspect ratio of the bubbles. The common understanding suggests that the aspect ratio is a universal constant independent of the bubble size. Here, by combining scanning tunneling microscopy and molecular dynamics, we show that the universal aspect ratio breaks down in MoS_2 nanobubbles below a critical radius (≈10 nm), where the aspect ratio increases with increasing size. Accordingly, additional atomic-level analyses indicate that the strain increases from 3% to 6% in the sub-critical size range. Using scanning tunneling spectroscopy, we demonstrate that the bandgap decreases as a function of the size. Thus, tunable quantum emitters can be obtained in 2D semiconductors by controlling the radius of the nanobubbles.

npj 2D Materials and Applications (2023)7:71 ; https://doi.org/10.1038/s41699-023-00432-x

INTRODUCTION

The advent of semiconducting honeycomb-structured transition-metal dichalcogenide (TMDC) membranes has stimulated significant research activity in the two-dimensional (2D) materials community[1]. Owing to their atomic-scale thickness and their beneficial electronic and optical properties, such as their direct band gap[2] and strong spin-orbit coupling[3], TMDCs are a promising alternative to graphene. Additionally, observations of single-photon emitters in various TMDCs suggest potential quantum applications[4]. This makes them appealing for fundamental studies as well as for electronics, spintronics, and optoelectronics applications (see recent reviews[1,4] and citations within).

In the TMDC family, molybdenum disulfide is the most studied material because it can be synthesized in single layers, it is relatively stable in air, and its band gap (1.86 eV) is larger than that of silicon (1.12 eV)[2], which is advantageous for low-power transistors[5]. Additionally, because of its 2D nature, its electronic properties can be easily tailored by strain engineering.[6,7] Moderate biaxial tensile strains (~2%) can decrease the bandgap size and trigger a direct-to-indirect bandgap transition[8–10]. At larger levels of strain (~10%), first-principle calculations predict the closure of the bandgap, thus leading to a semiconductor-to-metal transition[9,11].

For designing devices with bespoke properties, the creation of van der Waals (vdW) heterosystems has recently attracted considerable research interest because of their potential application in different fields[12–14]. The formation of a vertical interface can modify the electronic and magnetic properties of a membrane and induce exotic physical phenomena such as superconductivity in twisted bilayer graphene (tBLG)[15], the anomalous quantum Hall effect in tBLG aligned to hexagonal boron nitride (hBN)[16], or Mott-like states in $MoSe_2$/hBN/$MoSe_2$[17]. At the same time, obtaining 2D materials with large areas is essential for the assembly of real devices. In this context, the assembly of MoS_2 exfoliated on Au substrates is a model system. The relatively strong interaction of MoS_2 with Au leads to the exfoliation of high-quality monolayer membranes that exhibit a large area[18]. On (111)-oriented substrates, a moiré pattern develops at the MoS_2-Au interface, modulating the electronic properties of the surface through local variations in the MoS_2-Au bonds[19–21]. In particular, the hybridization of the S $3p_z$ orbitals with the Au *d* bands induces distortions in the valence band of MoS_2[20] and bandgap renormalization[21].

The adventitious contamination present on individual layers before the assembly of TMDC/substrate systems leads to the formation of stable bubbles with micro- and nanometer sizes[22]. The vdW forces that bind the adjacent layers facilitate the coalescence of trapped matter in minute bubbles, thus creating large inter-bubble areas that are atomically sharp and free of contamination via a process known as "self-cleansing"[23]. Recent investigations have shown that the presence of bubbles leads to variations in the local properties of 2D materials[24,25]. In addition, nanobubbles formed in different 2D heterostructures can serve as quantum-dot emitters because of the interplay between the strain-induced confinement[25] and changes in the local dielectric environment[26]. Notably, the aspect ratio between the height and radius of commonly occurring bubbles exhibits a universal scaling, which results from the balance between the membrane-substrate adhesion and the elastic properties of the membrane[22,27–29]. Detailed knowledge of the strain levels emerging in these bubbles is fundamental to understanding the local, strain-tunable electronic properties of monolayer TMDCs and related 2D materials.

In this study, we assess the shape and strain of intrinsic nanobubbles formed in MoS_2 monolayers exfoliated on Au(111). Room-temperature scanning tunneling microscopy (STM) is employed to obtain atomically resolved images of MoS_2 nanobubbles with radii of <25 nm. Our STM measurements show that, below a critical radius (≈10 nm), the MoS_2 bubbles exhibit decreasing aspect ratios with decreasing size. We compare our experimental results with molecular dynamics (MD) simulations, which support the aspect ratio scaling breakdown observed in our STM experiments. Our MD results also reveal the presence of ultra-

[1]J. Heyrovský Institute of Physical Chemistry, Czech Academy of Sciences, Dolejškova 2155/3, Prague 18223, Czech Republic. [2]Institute of Thermomechanics, Czech Academy of Sciences, Dolejškova 1402/5, Prague 18200, Czech Republic. [3]Materials Science Factory, Instituto de Ciencia de Materiales de Madrid, Consejo Superior de Investigaciones Científicas, Sor Juana Inés de la Cruz 3, Madrid 28049, Spain. [4]These authors contributed equally: Michele Gastaldo, Javier Varillas. ✉email: martin.kalbac@jh-inst.cas.cz

high pressures (up to 10 GPa) inside the smaller nanobubbles. Larger MoS_2 bubbles, conversely, exhibit pressures of the order of 100 MPa. The radial pair distribution function (RPDF) of the matter trapped inside the MD bubbles suggests a transition from a gas-like phase in larger nanobubbles to a liquid-like phase inside smaller bubbles. Additional atomic-level (STM and MD) analyses show that the strain follows the evolution of the aspect ratio, increasing with increasing bubble size from a minimum of ≈ 3% for the smallest bubbles. Above a critical radius of ≈10 nm, the strain stabilizes around a universal value as high as 8%. Strain maps also show the evolution of the local strain in the bubbles. The tunability of the strain is additionally supported by scanning tunneling spectroscopy (STS) measurements of the bandgap in MoS_2 nanobubbles. Our measurements indicate a bandgap decrease rate of approximately −140 meV per % strain in bubbles with radii of <10 nm.

RESULTS

STM measurements of MoS_2 nanobubbles

The nanobubbles are analyzed using STM topographic images of MoS_2 monolayers exfoliated using the gold-assisted method[18] on Au(111) films grown on mica (see Methods). The samples are prepared in air and then transferred to ultra-high vacuum (UHV). We find that annealing at 400 K is sufficient to desorb most contaminants and obtain high-resolution STM images, as shown in Fig. 1.

Figure 1a shows the topographic scan of a 70 nm × 70 nm area displaying a continuous moiré pattern that is indicative of MoS_2-covered Au terraces[30,31]. The nanobubbles are imaged as bright protrusions, which are predominantly found at the step edges of the Au substrate. This is consistent with the generally accepted notion that the bubbles originate from molecules trapped between the 2D membrane and the substrate, as the step edges are the energetically favored adsorption sites. The coverage of the protrusions on the surface ranges between 2% and 6%. In magnified STM scans, as shown in Fig. 1b, the atomic structure of MoS_2 nanobubbles is resolved. We observe a hexagonal lattice that is consistent with that of the top S atoms in 2H-MoS_2[32,33]. Although the moiré pattern is visible on the adjacent terrace (Fig. 1a), no superstructure is observed on the bubbles by STM (Fig. 1b). This confirms the decoupling of MoS_2 from the Au substrate over the nanobubble area. The interatomic distances, which measure 3.17 ± 0.03 Å on the moiré-characterized regions, range between 2.9 Å and 3.5 Å on the surface of the bubbles. The variation in these distances is due to local variations in strain, as we discuss below.

The bubbles exhibit elliptical/lenticular shapes and bell-like profiles (Fig. 1c). We measure their maximum height, h, and radius, R, along their longest axis. To ensure consistent measurements for nanobubbles formed at step edges and on terraces, we consider all bubbles as only being formed on the highest adjacent terrace. That is, for bubbles formed at step edges, h and R are measured by projecting the level of the highest terrace to the other side of the bubble (see Fig. 1c). Then, we obtain the aspect ratio, h/R, which is shown as a function of R for more than 170 bubbles in Fig. 1d. For $R > 10$ nm, the aspect ratio measured by STM exhibits a plateau at $h/R = 0.21 \pm 0.01$. The plateau is consistent with the universal scaling of bubbles demonstrated using different 2D materials, where the h/R value is determined solely by the adhesion energy and mechanical properties of the membrane[22]. We confirm this h/R value for large bubbles by atomic force microscopy (AFM) at ambient pressure ($h/R = 0.22 \pm 0.02$), thus excluding any influence of the external pressure or apparent height effects in the STM measurements (see Supplementary Note 1).

In bubbles with $R \leq 10$ nm, we find h/R values that decrease with decreasing R. The lowest h/R value found in our experiments is 0.07 for the smallest bubbles ($R \approx 2$ nm). Thus, the universal scaling of the aspect ratio appears to break down for small nanobubbles with sizes well below those investigated by Khestanova et al.[22]. We define a critical radius, R_c, below which the h/R breakdown occurs, and estimate it to be ≈10 nm from STM measurements.

We fit the profiles of the MoS_2 bubbles to the general shape proposed by Blundo et al.[27], where the height of the bubble, z, is defined as a function of the radial distance from the center, r, as $z(r) = h[1 - (r/R)^q]$. Fitting the profiles from different experimental and simulated large-sized bubbles ($R > 100$ nm) formed in monolayer membranes, Blundo et al. constructed a relation between h/R and the exponent q, whereby an exponent of $q \approx 2.3$ is expected for $h/R = 0.22$. In our MoS_2 bubbles, we find a value of $q \approx 2.3$ for $R > R_c$. This agreement indicates the absence of residual strain and defects in our membrane, as we would expect them to modify the shape of the nanobubbles. For smaller bubbles ($R < R_c$), we obtain lower values of q (as low as 1.83, see Supplementary Note 2 and Supplementary Table 1), which is consistent with the observed decrease in the h/R ratio in this regime.

MD simulations of MoS_2 nanobubbles

We perform all-atom MD simulations to study the formation of MoS_2 nanobubbles by employing the LAMMPS code[34]. Our computational setup is designed to capture the creation and relaxation of MoS_2 bubbles, in which a monolayer MoS_2 membrane is accommodated on top of a flat (111)-oriented Au substrate whose surface contains adhered contamination—modeled in our simulations as nitrogen atoms. During the relaxation, the contaminants trapped between the MoS_2 and the substrate (see Supplementary Fig. 3) form a MoS_2 bubble at the center of the periodic MoS_2/Au(111) system (see the Supplementary Video). For further details, see Methods and Supplementary Note 3.

We also simulate the formation of MoS_2 bubbles at Au(111) steps of monoatomic and biatomic height. Supplementary Note 4 provides a comparative analysis of relaxed MD bubbles with $R \approx$ 17 nm (where $R > R_c$) formed at Au step edges and on flat Au(111). According to our simulations, the resulting h/R is 0.20 and 0.22 when the bubble is formed at a biatomic step and on a flat surface, respectively. Thus, our MD results indicate that the maximum error in our experimental h/R measurements is ≈ 10% when comparing bubbles formed at steps and on a flat surface.

Figure 2a shows the profiles of relaxed MD bubbles for different R. Further fitting of the bubble profiles yields values of the exponent q that range from approximately 1.6 to 2.2 as h/R increases from approximately 0.12 to 0.21 (see Supplementary Table 1). In addition, our MD simulations clarify the role of the vdW-type adhesion between the membrane and the substrate in determining the resulting aspect ratio of relaxed bubbles. As expected, we find that increasing the adhesion between the MoS_2 and Au substrate, which was modeled using Lennard-Jones (LJ) potentials (see Supplementary Equation 3), gradually increases the aspect ratio of MoS_2 nanobubbles. Refer to Supplementary Notes 5–7 for further details.

Following the h/R evolution shown in Fig. 2b, our atomistic simulations also support the scaling breakdown revealed by the STM measurements for $R < R_c$. Our MD simulations indicate a slightly larger R_c (≈13 nm) than that observed in our STM analysis ($R_c \approx 10$ nm) (see Figs. 1d and 2b).

We map the evolution of the hydrostatic pressure of the trapped atoms, P, as a function of the MoS_2 nanobubble size. Supplementary Note 8 describes the approach we adopt to extract P from our MD simulations. The resulting evolution of P as a function of R shown in Fig. 2c indicates ultra-high pressures of up to 10 GPa inside MoS_2 bubbles with $R < 10$ nm. This is consistent

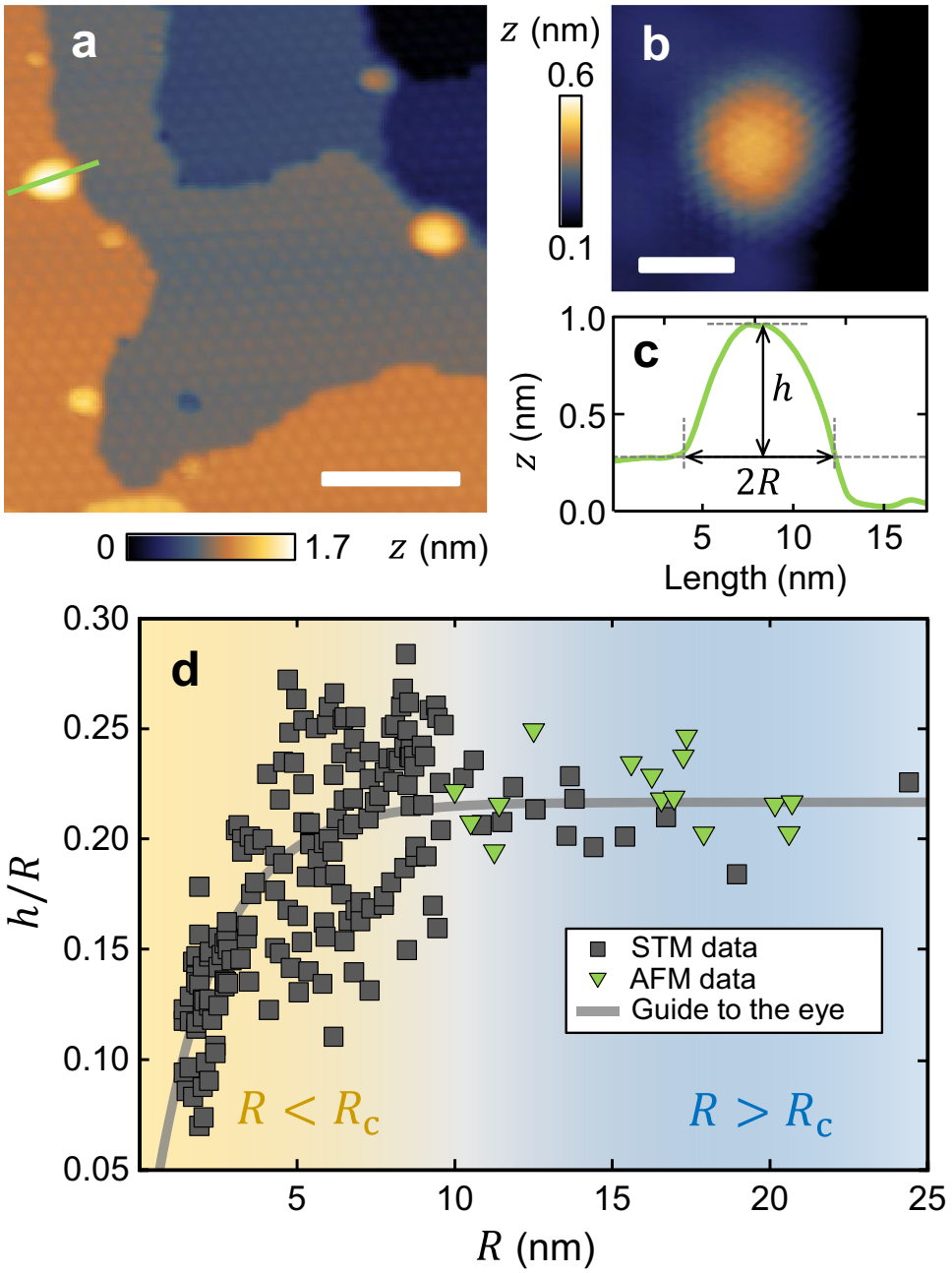

Fig. 1 STM measurements of MoS_2/Au(111) nanobubbles. a STM topography of monolayer MoS_2 exfoliated on Au(111) displaying the characteristic moiré-patterned terraces separated by monoatomic steps. The bright protrusions correspond to nanometer-sized MoS_2 bubbles. Setpoint for the measurement: bias voltage $V_{bias} = 1.5$ V, tunneling current $I_t = 0.3$ nA. Scale bar: 20 nm. **b** STM image of a MoS_2 nanobubble of $R = 1.9$ nm. Setpoint: $V_{bias} = 0.5$ V, $I_t = 0.6$ nA. Scale bar: 2 nm. **c** Profile of a MoS_2 nanobubble ($R = 4.2$ nm), marked with a green line in (**a**). **d** The evolution of h/R with R in MoS_2 nanobubbles as obtained by STM and AFM measurements. The gray line obtained by exponential regression provides a visual guide. Each data point corresponds to an individual MoS_2 bubble.

with previous reports on graphene nanobubbles of comparable size[35,36]. P levels are reduced toward pressures on the order of 100 MPa when $R > 10$ nm (see the inset to Fig. 2c). A similar $P(R)$ behavior was confirmed in recent experimental and analytical studies of nanobubbles formed in diverse vdW heterosystems, where the pressure inside the nanobubbles is inversely proportional to h[22,37].

Figure 2d displays the RPDFs of the trapped atoms as a function of R. In general terms, the RPDF represents the probability of finding a particle at a distance r^* from a particle placed at position $r^* = 0$. The shape of the RPDF indicates the phase of the trapped material inside the MD nanobubbles. In this framework, the RPDFs plotted in Fig. 2d suggest the presence of an "ordered" liquid-like phase inside nanobubbles of small size, as evidenced by the second and third peaks[38] of the curves for $R < R_c$. The transition to the liquid phase in small nanobubbles is associated with the accumulation of extreme pressures ($P > 2$ GPa) inside the bubbles. Recent density functional theory (DFT) results for graphene nanobubbles support the evolution of the RPDFs with increasing P suggested by our MD results[37]. The RPDFs for $R > R_c$, where nanobubbles exhibit much lower P levels, tend to follow those usually found in disordered gas-like fluids, as indicated by the softening of the secondary peaks. These findings agree with the continuum analysis reported by Iakovlev et al.[39], which indicates

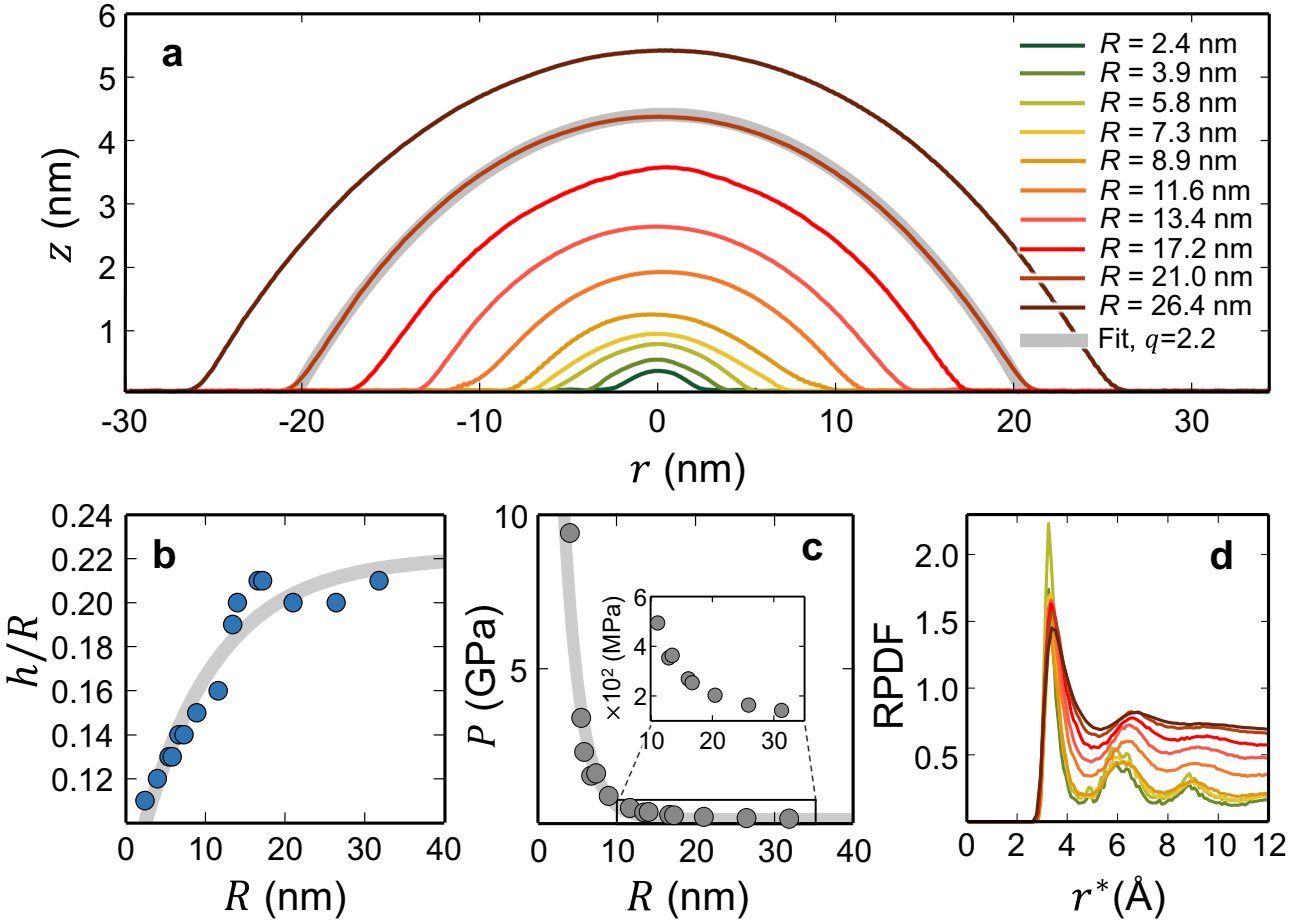

Fig. 2 Properties of MoS_2 nanobubbles obtained from MD simulations. a Bubble profiles with varying sizes, R. The profile for $R = 21.0$ nm is fitted by adopting the model proposed by Blundo et al.[27]. **b** Evolution of the h/R ratio as a function of R. **c** Calculated hydrostatic pressure, P, inside relaxed MoS_2 nanobubbles of different sizes (Supplementary Fig. 3). The gray line obtained by exponential regression provides a visual guide. Each data point in (**b**, **c**) accounts for one MD bubble. **d** RPDFs of the atoms trapped between the MoS_2 and the Au(111) substrate for different bubble sizes, where r^* stands for the distance from a reference atom[38] The color scheme follows that given in (**a**).

that gas-filled graphene nanobubbles develop a higher aspect ratio than liquid-containing ones.

Strain in MoS_2 nanobubbles

We calculate the local atomic-level strains, ε_{local}, across our relaxed MD nanobubbles by computing the individual atomistic displacements during the bubble formation and relaxation (Supplementary Note 9).

Figure 3a and b display the resulting ε_{local} maps from MoS_2 membranes containing small ($R < R_c$) and large ($R > R_c$) nanobubbles, respectively. Our ε_{local} maps from the MD simulations provide an indication for the formation of doughnut-like strain patterns in MoS_2 bubbles, where the ε_{local} global maxima are detected close to the bubble periphery and the local minima at the center; see the ε_{local} profile in Fig. 3c for a MD bubble of $R = 6.7$ nm. Our MD analysis also reveals that the development of such a strain pattern leads to a complex deformation state consisting of uniaxial, biaxial, and shear components (Supplementary Fig. 9).

Figure 3d shows the average strain, $\varepsilon_{bubble} = \langle \varepsilon_{local} \rangle$, obtained inside the simulated MoS_2 bubbles as a function of the radius, where $\langle \varepsilon_{local} \rangle$ denotes the average value of the ε_{local} data in the bubble. The average (in-bubble) strain gradually increases from ≈3% to ≈8% when R increases from 2.5 nm to R_c. STM measurements of the atomic-scale strains occurring in our experimental MoS_2 nanobubbles confirm the strain scaling found in our simulated bubbles with $R < R_c$. The strain estimation procedure in STM measurements of MoS_2 nanobubbles is described in Supplementary Note 11. For $R > R_c$, we obtain an average strain of ≈8%, which is found to be independent of R. Overall, these results evidence that the in-bubble strain scales with R in a similar manner to the aspect ratio (compare Fig. 3d and Fig. 1d).

In connection with this strain scaling, our MD results reveal that the ε_{local} distributions follow different shapes in the $R < R_c$ regime from those observed in the large-bubble (universal scaling) regime ($R > R_c$). In Fig. 3e, f, we plot together the estimated probability density functions (PDFs) of the ε_{local} data, as calculated by the Kernel density estimation. Note in these figures that subcritical-size MoS_2 nanobubbles tend to develop broad ε_{local} distributions (Fig. 3e), whereas the local strains of larger MD bubbles adhere to right-skewed distributions with a sharp peak at ≈$\langle \varepsilon_{local} \rangle$ (Fig. 3f).

Bandgap of MoS_2 nanobubbles

We acquire spectra near the center of 11 bubbles with different sizes and measure their local bandgap by STS. Because strain can be used to tune the bandgap size, the size of the bandgap can in turn be used to measure the strain.

The dI/dV spectra are shown in Fig. 4a. Here, the bandgap is identified as a region of zero conductance. The presence of this zero-signal region on top of bubbles confirms the decoupling of MoS_2 from the substrate, on which the strong MoS_2-Au hybridization normally manifests as a non-zero signal inside the

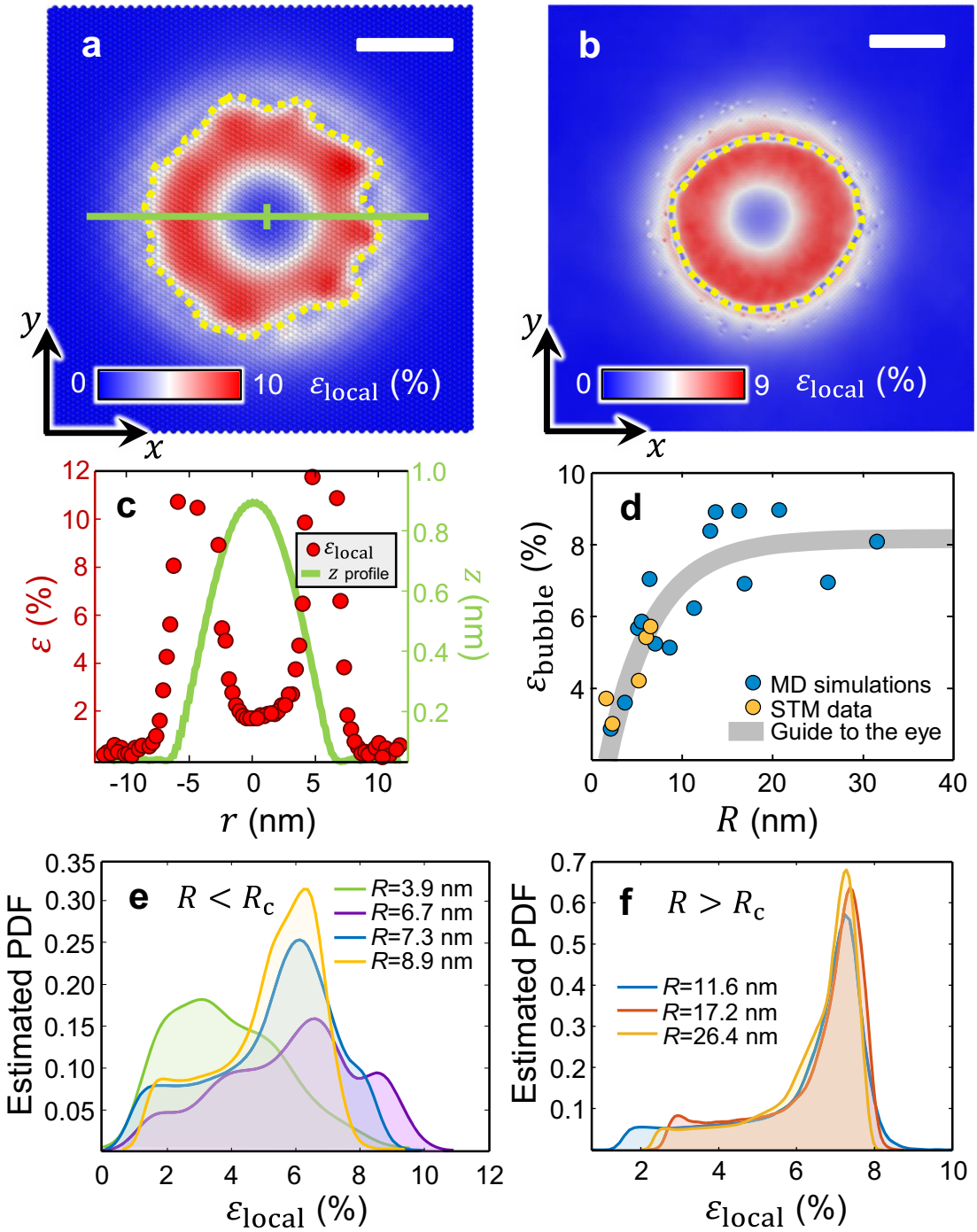

Fig. 3 Strain in MoS_2 nanobubbles. ε_{local} maps of MoS_2 from (**a**) 25 nm × 25 nm and (**b**) 130 nm × 130 nm periodic MD cells containing a relaxed bubble of $R = 6.7$ nm and $R = 26.4$ nm, respectively. For visual guidance, the bubble's perimeters are drawn in (**a**, **b**) with a dashed yellow contour. Scale bars: (**a**) 5 nm, (**b**) 20 nm. **c** Strain (ε) and height (z) profiles—marked with a green line in (**a**)—across the MoS_2 nanobubble ($R = 6.7$ nm). **d** ε_{bubble} vs. R obtained from STM and MD (see Supplementary Equation 12 for the details of the strain measurement by STM) The MD ε_{bubble} calculations correspond to the averaged (in-bubble) ε_{local} values obtained inside the MoS_2 bubbles. **e**, **f** The estimated probability density functions (PDFs) of the ε_{local} data from the simulated MoS_2 bubbles with $R < R_c$ ($R_{c,MD} \approx 13$ nm) and with $R > R_c$, respectively.

gap and leads to bandgap renormalization[21] (see Supplementary Note 12). Because the states far from the Γ point (such as those at the band edge of unstrained MoS_2) are difficult to detect by STS[20], we use the onsets of the tunneling conductance from its zero level on the two sides of the Fermi level as a measure of the bandgap edges. The measured bandgap corresponds to the quasiparticle bandgap, rather than the optical bandgap which is lowered by the exciton binding energy[40–42]. The energies of the conduction band minimum (CBM) and valence band maximum (VBM) are plotted as a function of R in Fig. 4b. The VBM upshifts in energy from approximately −1.6 to −1.4 eV with increasing R, whereas the CBM downshifts from approximately 0.6 to 0.4 eV. As a result, the local bandgap of our nanobubbles decreases from $E_g = 2.2$ eV for bubbles with $R = 2.4$ nm to ≈ 1.8 eV for those with $R = 7.9$ nm, as shown in Fig. 4c. The data are fitted to a linear regression, displayed as a visual guide in the figure. A linear approximation is

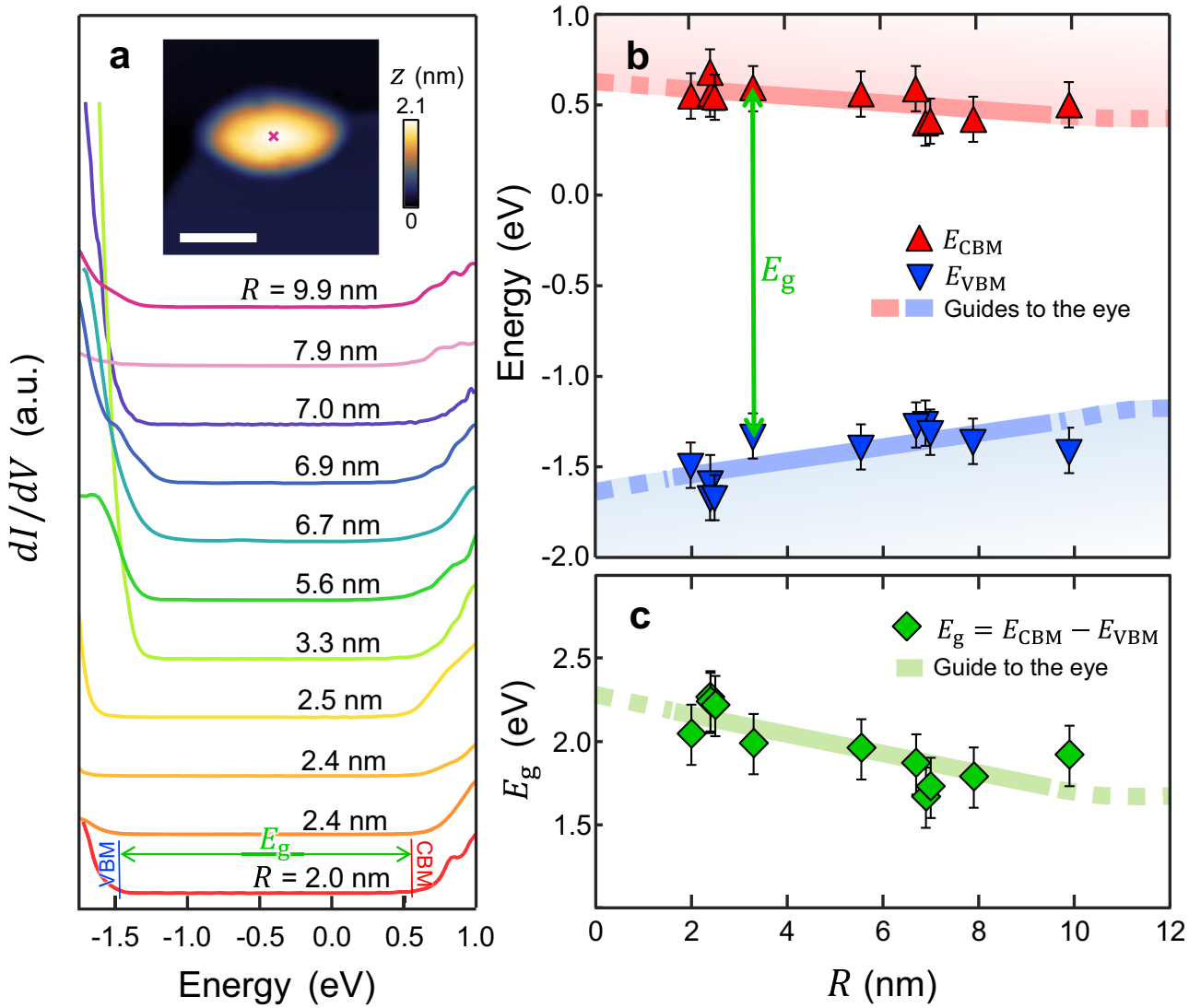

Fig. 4 Bandgap measurement by STS. a *dI/dV* spectra acquired near the center of 11 nanobubbles of increasing radii. The inset (scale bar: 10 nm) is a representative STM image of a bubble ($R = 9.9$ nm), and the location of the tip for the measurements is marked with a cross. Two spectra with different tip apexes are shown for a bubble of $R = 2.4$ nm. The setpoint for the measurements was $V_{bias} = 1.0$–1.2 V, $I_t = 0.5$ nA. **b** The energy of the valence and conduction band onsets extracted from the *dI/dV* spectra, as shown in (**a**) for the bubble of $R = 2$ nm. **c** The calculated bandgap ($E_g = E_{CBM} - E_{VBM}$) as a function of R. Notice that, for $R > 10$ nm, stabilization at a constant value is expected. The error bars in (**b**) and (**c**) are defined as $\Delta E = \sqrt{(3.3k_BT)^2 + (2.5V_{mod})^2}$, where k_B is the Boltzmann constant, T temperature, and V_{mod} (= 30 mV) the lock-in modulation signal.

consistent with the evolution of ε_{bubble} with increasing R for $R < 10$ nm (see Fig. 3f), whereas a plateau is expected for larger R.

We acknowledge that the large error in our room temperature STS measurements is mainly due to thermal broadening, $\Delta E = \sqrt{(3.3k_BT)^2 + (2.5V_{mod})^2} = 0.125$ eV, where the thermal broadening of $3.3\,k_BT$ accounts for approximately 0.09 eV at $T = 300$ K (k_B is the Boltzmann constant) and $V_{mod} = 30$ mV is the modulation applied to the bias. Two measurements on the same bubble of radius $R = 2.4$ nm (Fig. 4) indicate the magnitude of our error.

DISCUSSION

In large bubbles formed in 2D materials, a constant aspect ratio is determined solely by the balance between the substrate-2D membrane adhesion and mechanical properties of the membrane[22]. However, in the STM experiments and MD simulations, we find that this universal scaling is broken for MoS_2 nanobubbles with $R < R_c$, which exhibit lower aspect ratios. At a first glance, such behavior may be regarded as a nanoscale effect caused by the increasing edge-to-bulk ratio (the 2D equivalent of the surface-to-volume ratio) as the bubble size decreases. Here, the relevant edge and bulk effects would be the membrane-substrate adhesion and the bending rigidity of the membrane, respectively. However, the adhesion tends to minimize R and the bending rigidity limits the membrane curvature and h. Hence, in this simplified scenario, greater h/R values would be expected when the bubble size decreases. This is opposite to our observations for $R < R_c$.

Turning to membrane theory, the aspect ratio of the bubbles is driven by the minimization of the total energy, $E_{tot} = E_{bend} + E_{el} + E_b + E_{vdW}$. Here, E_{bend} is the out-of-plane bending energy, E_{el} is the in-plane elastic energy of the membrane, E_b is the free energy of the trapped substance, and E_{vdW} is the energy required to separate the membrane and substrate. The universal aspect

ratio (expressed as $h/R = (\pi\gamma/5c_1Y)^{1/4}$, where γ is the total adhesion, Y is Young's modulus, and c_1 is a constant) is valid above a critical size, where the bending rigidity of the membrane can be neglected[22]. At smaller sizes, however, the minimization of the total energy is determined by the bending rigidity term. As a result, for small radii, the $h(R)$ relation shifts from a linear dependency to a higher-order one[22,35].

Along these lines, a model derived by Lyublinskaya et al.[43] predicts an R-dependent aspect ratio evolution in small bubbles. Using non-linear plate theory and membrane theory, the authors showed that the energy minimization is dominated by the bending term below a critical radius that depends on temperature. This leads to a $h/R \sim R$ dependence followed by a $h/R \sim R^{1-\eta/2}$ one (with $\eta = 0.8$ for a 2D membrane) in the small-size limit. For radii above R_c, the bending energy is renormalized and the energy minimization is dominated by the elastic energy. In this range, the h/R ratio is determined by the pressure-induced tension (tension-dominated regime), which leads to the well-established universal scaling[43]. Hence, in the context of membrane theory, the scaling breakdown observed in our MoS_2 nanobubbles is explained by the onset of the bending-dominated regime for $R < R_c$.

Notably, by combining STM experiments and MD simulations, Villarreal et al.[35] reported an opposite behavior at very low radii, observing increasing h/R ratios as the bubble size decreases. Their nanobubbles (0.5 nm < R < 3 nm) are formed by sputtering noble-gas atoms through a graphene layer grown on Pt(111). However, in this system, a minimum bubble height, corresponding to a monolayer of trapped gas, is obtained for $R > R_c$ ($R_c \approx 0.4$ nm for graphene). The aspect ratio enters a $h/R \propto 1/R$ regime rather than the bending-dominated one, and, therefore, the breakdown observed in this case has a different origin.

Our STM measurements and MD simulations also demonstrate an increase in strain with increasing sizes of nanobubbles for $R < R_c$. Although the computational costs and the constraints on STM resolution (see Supplementary Note 11) limit the number of data points at larger radii, the average strain appears to reach a plateau centered at $\varepsilon_{bubble} = 8.2 \pm 0.9\%$. This is consistent with the strain scaling as $\varepsilon \propto h^2/R^2$ in bubbles formed in 2D materials[22] (see Figs. 1d and 2b). In a similar MoS_2/Au(111) system, Pető et al.[8] found the best fit for their Raman spectra and the bandgap measured by STS for a biaxial strain of 2% applied to flat MoS_2. However, our MD analyses of strain (Supplementary Fig. 9) indicate that MoS_2 nanobubbles exhibit a complex distribution of deformation states that differ from the purely biaxial scenario proposed by Pető et al.[8]. Thus, the combination of first-principles simulations and Raman measurements may lead to a misestimation of the average strain in nanobubbles. Recent studies also reported lower characteristic values of strain ($\varepsilon_{bubble} \approx 0.6$–2%) in large MoS_2 bubbles, obtained by photoluminescence (PL) and Raman spectroscopy[24] or mechanical models[22,44]. Similar values were also found in WS_2[29,45]. This discrepancy might be due to the PL/Raman spot size that is often close to one micrometer, which is larger than the typical size of bubbles formed in 2D materials. Thus, averaging with the flat, unstrained membrane must be considered. This idea is supported by our complementary simulations of the strain-induced Raman E mode shift distribution, which compare the spectra of flat MoS_2 areas that contain bubbles with bubble-only areas (see Supplementary Note 13). Furthermore, using STM topographies of nanobubbles, much higher strains (≈10%) have been reported[35]. We note that the breaking point of pristine MoS_2 layers is ≈11%[46], although lower values have been reported[47].

In addition, our simulations reveal that the spontaneous formation of MoS_2 nanobubbles leads to non-uniform strain distributions characterized by a doughnut-like shape, where the strain maxima are located close to the bubble periphery and the local minima at the center (Fig. 3a, b). Interestingly, we find that the formation of these "strain doughnuts" occurs regardless of R in MoS_2 nanobubbles with radii ranging from ≈2.5 nm to ≈32 nm. Similar strain patterns have been recently reported for MoS_2[26], WS_2[29], and WSe_2[25,48] nanobubbles. However, it is relevant to point out that elasticity theory predicts the strain maxima to be located at the top of bubbles[22,24,49,50]; see the $\varepsilon_{rr}(r)$ profile of Supplementary Fig. 2c in Ref. [50]. The discrepancy between the radial strain profiles described by such analytical solutions and those observed in our nanobubbles can be attributed to the elastic properties of MoS_2 at the nanoscale. In this regard, Carmesin et al.[26] interpret the formation of doughnut-shaped strain distributions in MoS_2 nanobubbles as the result of the high Young's modulus and localized bond deformations, which are not captured by classical elasticity theory[51].

In relation to bandgap engineering of TMDC membranes, recent studies have unveiled the presence of localized strains in various 2D/3D hybrid systems containing a 2D material coupled to a highly adhesive (3D) substrate with a patterned nanopillar array[52,53] or with nanoparticles[54], both leading to predictable quantum emissions. This localized quantum behavior observed in TMDCs is believed to be caused by the presence of non-uniform strain fields. However, the strain distribution in such 2D/3D heterosystems differs from that of commonly occurring nanobubbles. In the former, the local strain concentrations are governed by the topography of the interface between the membrane and the adhesive substrate, whereas the strain distributions obtained in our MD nanobubbles (Fig. 3a, b) originate from the competition among the thermodynamic equilibrium of the trapped matter, the elastic properties of the membrane, and the adhesion energy between the substrate and the 2D material.

Combining the STS data with our strain analyses, we estimate a decrease rate in the bandgap as a function of bubble size of approximately $-70\ \mathrm{meV\,nm^{-1}}$ for $R < R_c$ (2 nm ≤ R ≤ 8 nm). The strain increases linearly by ≈3% in the same R range (see Fig. 3f), which yields a bandgap decrease rate of approximately −140 meV per % strain for $R < R_c$. This value agrees well with the −124 meV per % strain recently obtained by combining PL measurements and DFT calculations[7] and is in overall agreement with other reported bandgap decrease rates under biaxial strain (ranging between −45 and −99 meV per % strain for the optical bandgap measured by PL[24,47,55] and between −190 and −230 meV per % strain for the indirect bandgap obtained from DFT calculations[8,56]). For MoS_2 under uniaxial strain, rates as high as −136 meV per % strain were observed by combining PL/Raman measurements and DFT calculations[57]. In the regime of linearly increasing strain obtained from the STM measurements and MD simulations for $R < R_c$, our STS analysis confirms a continuous tuning of the bandgap with increasing bubble size. We expect the bandgap size to reach a constant minimum for $R > R_c$, following the evolution of the strain with an inverse slope. Thus, the results in this work show that, in the subcritical size limit ($R < R_c$), the strain and bandgap of the nanobubbles can be tailored by controlling their size.

METHODS

Experimental

MoS_2 was exfoliated on Au(111) using a preparation method that predominantly yields monolayer flakes with sizes of at least hundreds of micrometers[18]. The samples were prepared at ambient pressure by flame-annealing the gold substrates (300 nm epitaxial Au(111) grown on mica, Georg Albert PVD, Heidelberg, Germany) and exfoliating a freshly cleaved MoS_2 crystal on top of it in rapid sequence. The samples were analyzed using an optical microscope to ensure sufficient MoS_2 coverage before being placed into a UHV chamber (with a pressure < 1×10^{-10} mbar), minimizing their exposure to ambient air to just a few minutes. To remove contamination from the

surface while preventing structural modifications or the creation of defects[58], the MoS_2/Au(111) samples were annealed at a low temperature (400 K) for one hour before each STM measurement. STM was performed at room temperature using a variable-temperature SPECS SPM Aarhus 150 equipped with a tungsten tip. To ensure consistent measurements of R and h, we only considered images with lateral sizes of 100–150 nm acquired at bias voltages of 1–1.5 V. The former requirement is necessary to avoid different non-linear background effects due to long-range scanning, and the latter is required to exclude offsets due to bias-dependent apparent heights (Supplementary Note 1). The post-processing and analysis of the STM images were carried out using Gwyddion software (http://gwyddion.net)[59].

Computational

We constructed MD cells containing the MoS_2/Au(111) hetero-system with characteristic areas ranging from 10 nm × 10 nm to 140 nm × 140 nm (see Supplementary Table 2). The as-built MoS_2 membranes have a bell-like shape that allows the introduction of trapped atoms between the MoS_2 and the Au substrate (see Supplementary Figs 3a and 3b). Periodic boundary conditions are imposed on the two sides of the computational domains, whereas the top and bottom walls are non-periodic. The fixed vertical dimension of the MD cells is set to h_0+ 20 Å, where h_0 is the height of the as-built MoS_2 bell. Additional details of MD cell construction are provided in Supplementary Note 3.

To describe the intralayer atomic interactions in the MoS_2 membranes, we use the reactive atomic bond order potential parameterized by Liang et al.[60], which generates consistent results with those from DFT calculations. The Au substrate is composed of two rigid, (111)-oriented atomic layers with a face-centered cubic lattice parameter of $a = 4.08$ Å[61]. The atomic interactions in the substrate are excluded from the calculations so that the positions of Au atoms remain fixed during the MD simulations. We choose N atoms to simulate the trapped contamination between the MoS_2 membrane and the Au substrate. The interatomic forces inside the bubbles are modeled using the 12–6 LJ potential (see Supplementary Note 5 and Supplementary Table 4). We also employ this model to describe the interactions between the trapped atoms with the MoS_2 membrane and the Au substrate, where the cross LJ parameters are obtained using the Waldman-Hagler mixing rules; see Supplementary Equations 4 and 5. The MoS_2 membrane and the Au(111) substrate mutually adhere through weak vdW forces that are also described by the LJ potential. The employed LJ values lead to ultra-high adhesion energies between the MoS_2 and Au(111) (see Supplementary Note 7). The LJ cutoff distance is set to 9 Å.

The energy of the as-built MoS_2/N/Au(111) system (Supplementary Fig. 3a) is initially minimized using the conjugate gradient method. Then, the system is relaxed over a 500-ps run. The dynamics of the trapped atoms follow the microcanonical *NVE* ensemble whereas the atoms of the MoS_2 membrane follow the canonical *NVT* ensemble with the Nosé-Hoover thermostat maintaining the temperature of MoS_2 at approximately 300 K. The computational timestep is set to 0.5 fs. Atomic visualization and data analysis of the MD results are conducted using the OVITO package (www.ovito.org)[62].

DATA AVAILABILITY

The data that support the findings of this study are available from the corresponding author upon reasonable request.

CODE AVAILABILITY

The codes that are necessary to reproduce the findings of this study are available from the corresponding author upon reasonable request. All MD simulations were carried out using the open-source LAMMPS code.

Received: 5 May 2023; Accepted: 11 September 2023;
Published online: 05 October 2023

REFERENCES

1. Manzeli, S., Ovchinnikov, D., Pasquier, D., Yazyev, O. V. & Kis, A. 2D transition metal dichalcogenides. *Nat. Rev. Mater.* **2**, 17033 (2017).
2. Mak, K. F., Lee, C., Hone, J., Shan, J. & Heinz, T. F. Atomically thin MoS_2: a new direct-gap semiconductor. *Phys. Rev. Lett.* **105**, 136805 (2010).
3. Xiao, D., Liu, G.-B., Feng, W., Xu, X. & Yao, W. Coupled spin and valley physics in monolayers of MoS_2 and other group-VI dichalcogenides. *Phys. Rev. Lett.* **108**, 196802 (2012).
4. Ren, S., Tan, Q. & Zhang, J. Review on the quantum emitters in two-dimensional materials. *J. Semicond.* **40**, 071903 (2019).
5. Dankert, A., Langouche, L., Kamalakar, M. V. & Dash, S. P. High-performance molybdenum disulfide field-effect transistors with spin tunnel contacts. *ACS Nano* **8**, 476–482 (2014).
6. Datye, I. M. et al. Strain-enhanced mobility of monolayer MoS_2. *Nano Lett.* **22**, 8052–8059 (2022).
7. Michail, A. et al. Biaxial strain engineering of CVD and exfoliated single- and bi-layer MoS_2 crystals. *2D Mater.* **8**, 015023 (2021).
8. Pető, J. et al. Moderate strain induced indirect bandgap and conduction electrons in MoS_2 single layers. *npj 2D Mater. Appl.* **3**, 39 (2019).
9. Yun, W. S., Han, S. W., Hong, S. C., Kim, I. G. & Lee, J. D. Thickness and strain effects on electronic structures of transition metal dichalcogenides: 2H-MX_2 semiconductors (M = Mo, W; X = S, Se, Te). *Phys. Rev. B* **85**, 033305 (2012).
10. Peelaers, H. & Van De Walle, C. G. Effects of strain on band structure and effective masses in MoS_2. *Phys. Rev. B Condens. Matter.* **86**, 241401 (2012).
11. Scalise, E., Houssa, M., Pourtois, G., Afanas'ev, V. & Stesmans, A. Strain-induced semiconductor to metal transition in the two-dimensional honeycomb structure of MoS_2. *Nano Res.* **5**, 43–48 (2012).
12. Geim, A. K. & Grigorieva, I. V. Van der Waals heterostructures. *Nature* **499**, 419–425 (2013).
13. Zhang, W., Wang, Q., Chen, Y., Wang, Z. & Wee, A. T. S. Van der Waals stacked 2D layered materials for optoelectronics. *2D Mater.* **3**, 022001 (2016).
14. Liu, Y. et al. Van der Waals heterostructures and devices. *Nat. Rev. Mater.* **1**, 16042 (2016).
15. Cao, Y. et al. Unconventional superconductivity in magic-angle graphene superlattices. *Nature* **556**, 43–50 (2018).
16. Serlin, M. et al. Intrinsic quantized anomalous hall effect in a moiré heterostructure. *Science* **367**, 900–903 (2020).
17. Shimazaki, Y. et al. Strongly correlated electrons and hybrid excitons in a moiré heterostructure. *Nature* **580**, 472–477 (2020).
18. Velický, M. et al. Mechanism of gold-assisted exfoliation of centimeter-sized transition-metal dichalcogenide monolayers. *ACS Nano* **12**, 10463–10472 (2018).
19. Silva, C. C. et al. Spatial variation of geometry, binding, and electronic properties in the moiré superstructure of MoS_2 on Au(111). *2D Mater.* **9**, 025003 (2022).
20. Krane, N., Lotze, C. & Franke, K. J. Moiré structure of MoS_2 on Au(111): local structural and electronic properties. *Surf. Sci.* **678**, 136–142 (2018).
21. Bruix, A. et al. Single-layer MoS_2 on Au(111): band gap renormalization and substrate interaction. *Phys. Rev. B* **93**, 165422 (2016).
22. Khestanova, E., Guinea, F., Fumagalli, L., Geim, A. K. & Grigorieva, I. V. Universal shape and pressure inside bubbles appearing in van der Waals heterostructures. *Nat. Commun.* **7**, 12587 (2016).
23. Fan, S., Vu, Q. A., Tran, M. D., Adhikari, S. & Lee, Y. H. Transfer assembly for two-dimensional van der Waals heterostructures. *2D Mater.* **7**, 022005 (2020).
24. Tyurnina, A. V. et al. Strained bubbles in van der Waals heterostructures as local emitters of photoluminescence with adjustable wavelength. *ACS Photonics* **6**, 516–524 (2019).
25. Darlington, T. P. et al. Imaging strain-localized excitons in nanoscale bubbles of monolayer WSe_2 at room temperature. *Nat. Nanotechnol.* **15**, 854–860 (2020).
26. Carmesin, C. et al. Quantum-dot-like states in molybdenum disulfide nanostructures due to the interplay of local surface wrinkling, strain, and dielectric confinement. *Nano Lett.* **19**, 3182–3186 (2019).
27. Blundo, E., Yildirim, T., Pettinari, G. & Polimeni, A. Experimental adhesion energy in van der Waals crystals and heterostructures from atomically thin bubbles. *Phys. Rev. Lett.* **127**, 046101 (2021).
28. Jain, S. K., Juričić, V. & Barkema, G. T. Probing the shape of a graphene nanobubble. *Phys. Chem. Chem. Phys.* **19**, 7465–7470 (2017).
29. Jia, Z. et al. Photoluminescence and raman spectra oscillations induced by laser interference in annealing-created monolayer WS_2 bubbles. *Adv. Opt. Mater.* **7**, 1801373 (2019).

30. Sørensen, S. G., Füchtbauer, H. G., Tuxen, A. K., Walton, A. S. & Lauritsen, J. V. Structure and electronic properties of in situ synthesized single-layer MoS_2 on a gold surface. *ACS Nano* **8**, 6788–6796 (2014).
31. Grønborg, S. S. et al. Synthesis of epitaxial single-layer MoS_2 on Au(111). *Langmuir* **31**, 9700–9706 (2015).
32. Altibelli, A., Joachim, C. & Sautet, P. Interpretation of STM images: the MoS_2 surface. *Surf Sci.* **367**, 209–220 (1996).
33. Helveg, S. et al. Atomic-scale structure of single-layer MoS_2 nanoclusters. *Phys. Rev. Lett.* **84**, 951–954 (2000).
34. Plimpton, S. Fast parallel algorithms for short-range molecular dynamics. *J. Comput. Phys.* **117**, 1 – 19 (1995).
35. Villarreal, R. et al. Breakdown of universal scaling for nanometer-sized bubbles in graphene. *Nano Lett.* **21**, 8103–8110 (2021).
36. Zamborlini, G. et al. Nanobubbles at GPa pressure under graphene. *Nano Lett.* **15**, 6162–6169 (2015).
37. Aslyamov, T. F., Iakovlev, E. S., Akhatov, I. S. & Zhilyaev, P. A. Model of graphene nanobubble: combining classical density functional and elasticity theories. *J. Chem. Phys.* **152**, 054705 (2020).
38. Ghosh, K. & Krishnamurthy, C. V. Structural behavior of supercritical fluids under confinement. *Phys. Rev. E* **97**, 012131 (2018).
39. Iakovlev, E. S., Zhilyaev, P. A. & Akhatov, I. S. Obtaining the state of matter inside graphene nanobubble from its shape. *J. Phys. Conf. Ser.* **1147**, 012006 (2019).
40. Huang, Y. L. et al. Bandgap tunability at single-layer molybdenum disulphide grain boundaries. *Nat. Commun.* **6**, 6298 (2015).
41. Ramasubramaniam, A. Large excitonic effects in monolayers of molybdenum and tungsten dichalcogenides. *Phys. Rev. B* **86**, 115409 (2012).
42. Shi, H., Pan, H., Zhang, Y.-W. & Yakobson, B. I. Quasiparticle band structures and optical properties of strained monolayer MoS_2 and WS_2. *Phys. Rev. B* **87**, 155304 (2013).
43. Lyublinskaya, A. A., Babkin, S. S. & Burmistrov, I. S. Effect of anomalous elasticity on bubbles in van der Waals heterostructures. *Phys. Rev. E* **101**, 033005 (2020).
44. Guo, Y. et al. Direct bandgap engineering with local biaxial strain in few-layer MoS_2 bubbles. *Nano Res.* **13**, 2072–2078 (2020).
45. Zhang, D. et al. Reconstructing local profile of exciton-emission wavelengths across a WS_2 bubble beyond the diffraction limit. *ACS Nano* **14**, 6931–6937 (2020).
46. Bertolazzi, S., Brivio, J. & Kis, A. Stretching and breaking of ultrathin MoS_2. *ACS Nano* **5**, 9703–9709 (2011).
47. Lloyd, D. et al. Band gap engineering with ultralarge biaxial strains in suspended monolayer MoS_2. *Nano Lett.* **16**, 5836–5841 (2016).
48. Rodríguez, A., Kalbáč, M. & Frank, O. Strong localization effects in the photoluminescence of transition metal dichalcogenide heterobilayers. *2D Mater.* **8**, 025028 (2021).
49. Dai, Z. et al. Interface-governed deformation of nanobubbles and nanotents formed by two-dimensional materials. *Phys. Rev. Lett.* **121**, 266101 (2018).
50. Rostami, H., Guinea, F., Polini, M. & Roldán, R. Piezoelectricity and valley chern number in inhomogeneous hexagonal 2D crystals. *npj 2D Mater. Appl.* **2**, 15 (2018).
51. Tapasztó, L. et al. Breakdown of continuum mechanics for nanometre-wavelength rippling of graphene. *Nat. Phys.* **8**, 739–742 (2012).
52. Li, H. et al. Optoelectronic crystal of artificial atoms in strain-textured molybdenum disulphide. *Nat. Comm.* **6**, 7381 (2015).
53. Palacios-Berraquero, C. et al. Large-scale quantum-emitter arrays in atomically thin semiconductors. *Nat. Comm.* **8**, 15093 (2017).
54. Kim, G. et al. High-density, localized quantum emitters in strained 2D semiconductors. *ACS Nano* **16**, 9651–9659 (2022).
55. Conley, H. J. et al. Bandgap engineering of strained monolayer and bilayer MoS_2. *Nano Letters* **13**, 3626–3630 (2013).
56. Feng, J., Qian, X., Huang, C.-W. & Li, J. Strain-engineered artificial atom as a broad-spectrum solar energy funnel. *Nat. Photon.* **6**, 866–872 (2012).
57. Li, Z. et al. Efficient strain modulation of 2D materials via polymer encapsulation. *Nat. Commun.* **11**, 1151 (2020).
58. Hus, S. M. et al. Observation of single-defect memristor in an MoS_2 atomic sheet. *Nat. Nanotechnol.* **16**, 58–62 (2021).
59. Nečas, D. & Klapetek, P. Gwyddion: an open-source software for SPM data analysis. *Open Phys.* **10**, 181–188 (2012).
60. Liang, T., Phillpot, S. R. & Sinnott, S. B. Parametrization of a reactive many-body potential for Mo–S systems. *Phys. Rev. B* **79**, 245110 (2009).
61. Zhou, X. W., Johnson, R. A. & Wadley, H. N. G. Misfit-energy-increasing dislocations in vapor-deposited CoFe/NiFe multilayers. *Phys. Rev. B* **69**, 144113 (2004).
62. Stukowski, A. Visualization and analysis of atomistic simulation data with OVITO-the open visualization tool. *Simul. Mater. Sci. Eng.* **18**, 015012 (2010).

ACKNOWLEDGEMENTS

M.G., A.R., O.F. and M.K acknowledge the support of the Czech Science Foundation, Project No. 20-08633X. M.V. and A.R. acknowledge the support of the Czech Science Foundation, Project No. GA22-04408S. J.V. acknowledges institutional support, RVO: 61388998. The funders played no role in study design, data collection, analysis and interpretation of data, or the writing of this manuscript.

AUTHOR CONTRIBUTIONS

M.G. and J.V contributed equally to this work. M.G. fabricated the samples and measured them by STM and STS. J.V. designed and analyzed the MD simulations. A.R. measured and analyzed the AFM data. M.V. supervised the sample fabrication and data analysis. O.F. and M.K. supervised the work. All authors contributed to the writing of the manuscript and to the discussion of the results.

COMPETING INTERESTS

The authors declare no competing interests.

ADDITIONAL INFORMATION

Supplementary information The online version contains supplementary material available at https://doi.org/10.1038/s41699-023-00432-x.

Correspondence and requests for materials should be addressed to Martin Kalbáč.

Reprints and permission information is available at http://www.nature.com/reprints

Publisher's note Springer Nature remains neutral with regard to jurisdictional claims in published maps and institutional affiliations.